ACS APPLIED MATERIALS & INTERFACES

Research Article

Cite This: ACS Appl. Mater. Interfaces 2018, 10, 19764−19772

www.acsami.org

Donor−Acceptor Supramolecular Organic Nanofibers as Visible-Light Photoelectrocatalysts for Hydrogen Production

Liping Yang,[†,‡] Maomao Wang,[†] Paul M. Slattum,[§,∥,⊥] Benjamin R. Bunes,[§,⊥] Yuanhao Wang,[*,†] Chuanyi Wang,[*,†,#] and Ling Zang[*,⊥]

[†]Laboratory of Environmental Science and Technology, The Xinjiang Technical Institute of Physics and Chemistry; Key Laboratory of Functional Materials and Devices for Special Environments, Chinese Academy of Sciences, Urumqi 830011, P. R. China

[‡]University of Chinese Academy of Sciences, Beijing 100049, P. R. China

[§]Vaporsens Inc., 36 South Wasatch Drive, Salt Lake City, Utah 84112, United States

[∥]Leibniz-Institut für Polymerforschung Dresden e.V., Hohe Straße 6, D-01069 Dresden, Germany

[⊥]Nano Institute of Utah and Department of Materials Science and Engineering, University of Utah, Salt Lake City, Utah 84112, United States

[#]School of Environmental Science and Engineering, Shaanxi University of Science & Technology, Xi'an 710021, China

Supporting Information

ABSTRACT: Perylene tetracarboxylic diimide (PTCDI) derivatives have been extensively studied for one-dimensional (1D) self-assembled systems and for applications in photocatalysis. Herein, we constructed a PTCDI-based donor−acceptor (D−A) supramolecular system via in situ self-assembly on an indium tin oxide conductive glass surface. The self-assembled PTCDI nanostructures exhibit well-defined nanofibril morphologies and strong photocurrents. Interestingly, a strong and reversible electrochromic color change was observed during cyclic voltammetry. The color of the nanofibers changed from red to blue and then to violet as the reduction progressed to the radical anion and then to the dianion. This series of one-electron reductions was confirmed by UV absorption, electron paramagnetic resonance spectroscopy, and hydrazine reduction. Most importantly, these PTCDI nanofibers exhibit efficient photoelectrocatalytic hydrogen production with remarkable stability under xenon lamp illumination ($\lambda \geq 420$ nm). Among the three nanofibers prepared, the fibers assembled from PTCDI molecule **2** were found to be the most effective catalyst with 30% Faradaic efficiency. In addition, the nanofibers produced hydrogen at a steady-state for more than 8 h and produced repeatable results in 3 consecutive testing cycles, giving them great potential for practical industrial applications. Under an applied bias voltage, the 1D intermolecular stacking along the long axis of the nanofibers affords efficient separation and migration of photogenerated charge carriers, which play a crucial role in the photoelectrocatalytic process. As a proof-of-concept, the D−A-structured PTCDI nanofibers presented herein may guide future research on photoelectrocatalysis based on self-assembled supramolecular systems by providing more options for material design of the catalysts to achieve greater efficiencies.

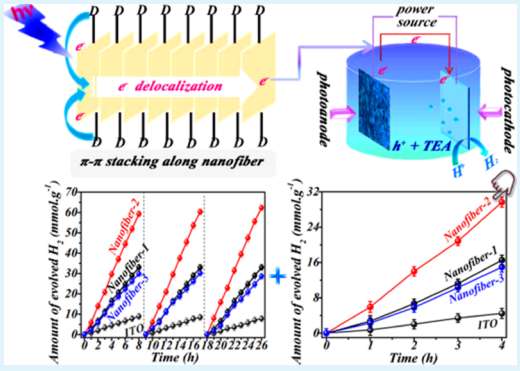

KEYWORDS: *one-dimensional self-assembly, photoelectrocatalyst, hydrogen production, nanofiber, perylene tetracarboxylic diimide*

1. INTRODUCTION

Compared with their inorganic counterparts, organic semiconductor materials possess unique advantages, including chemically tunable electronic and structural properties because of their structural diversity.[1−4] Small-molecule organic semiconductors have been used in various optoelectronic applications (including solar cells).[5−7] As in the case of organic photovoltaic, the photoinduced charge separation in donor−acceptor (D−A) materials plays a critical role in the photocatalytic system, wherein the free charges created at the surface initiate chemical reactions.[8−13] Nevertheless, fabrication of such effective D−A heterojunction structures for use in photocatalysis still remains a great challenge.

Molecules based on perylene tetracarboxylic diimide (PTCDI) form n-type semiconductors with excellent thermal and photostability, high electron affinity, and good charge carrier mobility.[14] The band gap of PTCDI molecules is approximately 2.5 eV, which closely matches the energy of visible light, and when these molecules are assembled into a

Received: April 10, 2018
Accepted: May 23, 2018
Published: May 23, 2018

DOI: 10.1021/acsami.8b05637
ACS Appl. Mater. Interfaces 2018, 10, 19764−19772

solid state, the band gap shrinks further with the absorption edge extending to 700 nm, resulting in more absorption in the visible range. PTCDI-based D−A molecules have been proven effective for applications in different optoelectronic systems.[15−17] The planar π-conjugation of the PTCDI core is conducive to cofacial $\pi-\pi$ molecular stacking, which favors one-dimensional (1D) self-assembly, resulting in well-defined nanofibril structures, which not only creates a large D−A interface for enhanced charge separation but also provides a continuous charge transport pathway (via cofacial intermolecular charge delocalization) for the photogenerated electrons, facilitating charge collection at the electrodes.[6,18−22]

The strong electron affinity of PTCDI makes it an efficient electron acceptor. Furthermore, an electron donor can be attached at the imide position without altering the electronic properties of the perylene core. The D−A molecules created in this manner can be assembled into nanofiber structures that function as effective photoconductive materials, as shown in recent studies.[23] The photogenerated electrons can move to the surface to initiate chemical reactions (i.e., photocatalysis[8,9,24,26]) or interact with the surface-adsorbed species (thus enabling chemiresistive sensing).[14,17,23,25] One way to enhance the charge separation (and thus photocatalysis) is to apply an external electrical bias to break the Coulombic interactions, shifting the electrons to a counter electrode, as previously evidenced in inorganic photocatalysts such as TiO_2,[27] *However, such photoelectrocatalysis involving organic photocatalysts has been studied much less largely because of the lack of suitable organic semiconducting materials.*[28]

Herein, we report three unique PTCDI-based D−A nanofibers that have demonstrated efficient photoelectrocatalytic hydrogen production from water. The three building block molecules (**1**, **2**, and **3** in Scheme 1) are all substituted with tertiary alkyl amines to ensure similar electron donating power. Self-assembly of the three molecules form shape-defined nanofibers with similar morphology and sizes, providing common ground for a comparative study of the photoelectrocatalysis. The same donor groups present on **1** and **2** were recently used as substituents in other PTCDI building blocks, and nanofibers formed from these molecules demonstrated efficient photoconductivity.[20,21] Building upon these initial successes, we aimed to in this study further enhance the charge separation by applying an external bias to the D−A material. Using platinum as the cathode, the photogenerated electrons can be driven to the electrode to initiate water reduction (production of hydrogen). The amount of hydrogen generated was quantitatively monitored to evaluate the hydrogen evolution kinetics in correlation with the different PTCDI catalysts. It is worthwhile to note that such detailed measurement of hydrogen production have only been reported on a small number of studies in organic photocatalysts.[8,29−33] Interestingly, the three nanofibers demonstrated significantly different efficiency in hydrogen production despite the same electron donor group (*N*-methyl piperidine). This is likely due to the different molecular stacking configurations, which affect the D−A charge transfer and separation, as well as the intermolecular charge delocalization (transport). The observation reported in this work helps open wide options for future study on the structure−property−function relationship of organic nanomaterials with regard to the molecular design for the efficiency enhancement of photoelectrocatalysis.

Scheme 1. Molecular Structures of PTCDI Derivatives Studied in This Work: 2,9-Bis[4-(dimethylamino)butyl]-3,4,9,10-perylene Tetracarboxylic Diimide (Molecule 1), 2,9-Bis[1-[(1-methyl-4-piperidyl)methyl]]-3,4,9,10-perylene Tetracarboxylic Diimide (Molecule 2) and 2,9-Bis[1-[(1-methyl-3-piperidyl)methyl]]-3,4,9,10-perylene Tetracarboxylic Diimide (Molecule 3)

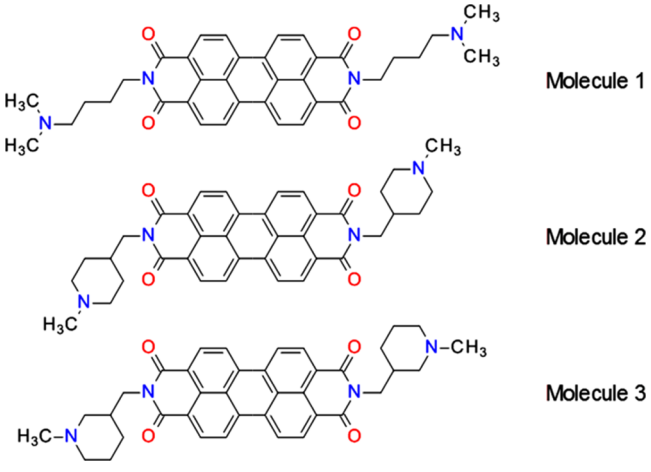

2. EXPERIMENTAL SECTION

2.1. Materials, Molecular Synthesis and Fabrication of Nanofibers. *2.1.1. Materials.* Chloroform, methane, triethanolamine (TEA), and hydrochloric acid were purchased from Adamas-beta. 3,4,9,10-Perylenetetracarboxylic acid dianhydride was purchased from Acros Organics, *N*,*N*-dimethyl-1,4-butanediamine was purchased from Sigma-Aldrich, and 4-(aminomethyl)-1-methylpiperidine and 3-(aminomethyl)-1-methylpiperidine were purchased from Matrix Scientific. All reagents were analytically pure and used without further purification.

2.1.2. Synthesis of PTCDI D−A Molecules. Three PTCDI molecules modified with different electron-donating groups (as shown in Scheme 1) were synthesized following literature methods.[14] The synthetic protocols and structural characterization using NMR and MS are briefly described below.

2.1.2.1. Molecule 1: 2,9-Bis[4-(dimethylamino)butyl]-3,4,9,10-perylene Tetracarboxylic Diimide. 3,4,9,10-Perylenetetracarboxylic dianhydride (1.12 g, 2.87 mmol) and *N*,*N*-dimethyl-1,4-butanediamine (1.0 g, 8.62 mmol) were combined along with zinc acetate (25 mg, 0.11 mmol) in imidazole (9 g). The reaction was heated to 110 °C under magnetic stirring for 4 h. The reaction mixture was then poured into 2 N HCl (50 mL). The resulting solution was neutralized with concentrated KOH. The neutralized mixture was extracted 4 × 250 mL of $CHCl_3$. The combined organic layers were washed 4 × 100 mL of water and 1 × 50 mL of brine and dried over Na_2SO_4. Solvent removal and vacuum drying yielded 1.53 g (2.6 mmol, 90.5%) of the product as a red solid. Mass spectra were obtained on a Bruker Daltonics UltrafleXtreme/MALDI/TOF. MS ($M + H^+$), *m*/*z*: 589.35 (calcd, 589.27). ^{1}H NMR (500 MHz, $CDCl_3$) ppm: 1.59−1.69 (m, 4H, $2N(CH_3)_2CH_2C\underline{H}_2$), 1.77−1.86 (m, 4H, $2N-(CH_3)_2CH_2CH_2C\underline{H}_2$), 2.25 (s, 12H, 4N-$C\underline{H}_3$), 2.36 (t, J = 7.30 Hz, 4H, $2N(CH_3)_2C\underline{H}_2$), 4.25 (t, J = 7.57 Hz, 4H, $2N-(CH_3)_2CH_2CH_2CH_2C\underline{H}_2$), 8.55 (d, J = 8.00 Hz, 4H, perylene), 8.64 (d, J = 8.00 Hz, 4H, perylene).

2.1.2.2. Molecule 2: 2,9-Bis[1-[(1-methyl-4-piperidyl)methyl]]-3,4,9,10-perylene Tetracarboxylic Diimide. 3,4,9,10-Perylenetetracarboxylic dianhydride (1.70 g, 4.40 mmol) and (1-methyl-4-piperidyl)-methanamine (1.7 g, 13.3 mmol) were combined along with zinc acetate (38 mg, 0.18 mmol) in imidazole (20 g). The reaction was heated to 110 °C under magnetic stirring for 4 h. The reaction mixture was then poured into 2 N HCl (100 mL). This suspension was diluted to approximately 1 L and filtered to remove insoluble impurities. The pH was adjusted to 10, and the precipitated product was isolated by

DOI: 10.1021/acsami.8b05637
ACS Appl. Mater. Interfaces 2018, 10, 19764−19772

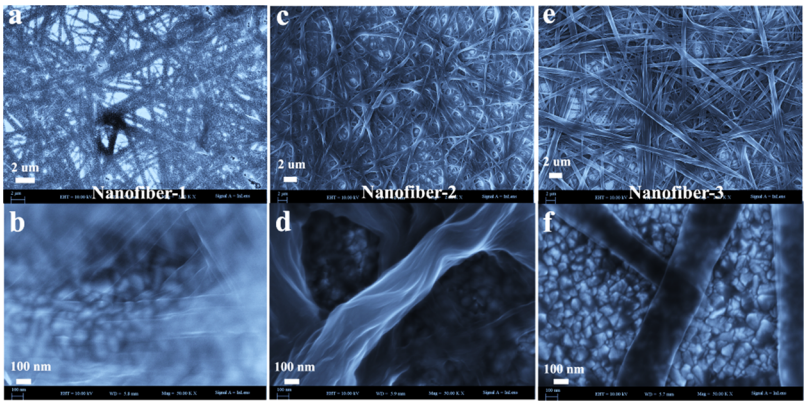

Figure 1. Large-area and zoom-in SEM images of the shape-defined nanofibers assembled from molecule **1** (a,b), **2** (c,d), and **3** (e,f).

filtration. The product was vacuum-dried and recrystallized from chloroform/methanol. Vacuum drying of the filtrate afforded 810 mg (1.32 mmol, 30.1%) of product as a red solid. Mass spectra were obtained on a Bruker Daltonics UltrafleXtreme/MALDI/TOF. MS ($M + H^+$), m/z: 613.31 (calcd, 612.27). ^{1}H NMR (500 MHz, $CDCl_3$) ppm: 1.26−1.35 (m, 2H, $2N(CH_3)CH_2CH_2CH_2CH$), 1.52−1.61 (m, 4H, $4N(CH_3)CH_2CH_{eq}$), 1.71−1.79 (m, 4H, $4N(CH_3)CH_2CH_{ax}$), 1.88−1.97 (m, 4H, $4N(CH_3)CH_{eq}$), 2.27 (s, 6H, $2N\text{-}CH_3$), 2.84−2.91 (m, 4H, $4N(CH_3)CH_{ax}$), 4.18 (d, J = 7.01 Hz, 4H, peryleneN-CH_2), 8.63 (d, J = 8.04 Hz, 4H, perylene), 8.70 (d, J = 8.04 Hz, 4H, perylene).

*2.1.2.3. Molecule **3**: 2,9-Bis[1-[(1-methyl-3-piperidyl)methyl]]-3,4,9,10-perylene Tetracarboxylic Diimide.* 3,4,9,10-Perylenetetracarboxylic dianhydride (2.04 g, 5.04 mmol) and (1-methyl-3-piperidyl)-methanamine (2.0 g, 15.6 mmol) were combined along with zinc acetate (45 mg, 0.208 mmol) in imidazole (20 g). The reaction was heated to 110 °C under magnetic stirring for 4 h. The reaction mixture was then poured into 2 N HCl (250 mL) and filtered to remove insoluble impurities. The filtrate was basified with concentrated KOH solution, which resulted in an emulsion. A solution was obtained by adding a mixture of chloroform and methanol (1:2 v/v). A 1:1 mixture of chloroform and methanol was added, and this addition resulted in the formation of two layers with the product in the chloroform layer. The chloroform layer was dried with Na_2SO_4. The solvent was removed, and the residue was recrystallized from chloroform/methanol. Vacuum drying of the filtrate afforded 2.74 mg (4.48 mmol, 88.8%) of product as a red solid. Mass spectra were obtained on a Bruker Daltonics UltrafleXtreme/MALDI/TOF. MS ($M + H^+$), m/z: 613.32 (calcd, 612.27). ^{1}H NMR (500 MHz, $CDCl_3$) ppm: 1.09−1.20 (m, 2H, $2N(CH_3)CH_2CH_2CH_2CH$), 1.24−1.31 (m, 2H, $2N(CH_3)CH_2CH_2CH_{eq}$), 1.55−1.67 (m, 2H, $2N(CH_3)CH_2CH_{eq}$), 1.72−1.79 (m, 2H, $2N(CH_3)CH_2CH_2CH_{ax}$), 1.80−1.87 (m, 2H, $2N(CH_3)CH_2CH_{ax}$), 1.87−2.01 (m, 4H, $4N(CH_3)CH_{eq}$), 2.26 (s, 6H, $2N\text{-}CH_3$), 2.74−2.86 (m, 4H, $4N(CH_3)CH_{ax}$), 4.12−4.19 (m, 4H, peryleneN-CH_2), 8.64 (d, J = 8.08 Hz, 4H, perylene), 8.70 (d, J = 8.08 Hz, 4H, perylene).

2.1.3. Preparation of PTCDI D−A Nanofibers. Nanofibers were prepared from 10 mL of the stock solution of PTCDI (1.0 mM) in chloroform. The solution was clear and red in color. PTCDI molecules **1**−**3** were self-assembled in a closed container using a solvent-vapor diffusion process resulting in in situ self-assembly on the surface of indium tin oxide (ITO) conductive glass, which served as the substrate. Specifically, a solid screw-cap (the diameter is 25 mm) containing 1 × 1 cm^2 ITO conductive glass was placed in a crystallizing dish (150 mm), and 40 mL of methanol was injected along the wall of the container to allow the screw cap to float on the methanol liquid. Then, 100 μL of the PTCDI stock solution was slowly drop-cast onto the ITO conductive glass surface to prevent liquid spillover. Following the addition of the PTCDI, the container was rapidly sealed with a sealing film, cling film, and rubber band, and the samples were transferred to a constant temperature oven held at 30 °C for 24 h to allow in situ self-assembly of the PTCDI molecules into nanofibers. Finally, the nanofibers formed on the ITO substrate were dried in a vacuum oven at 50 °C for 30 min. The self-assembly process is driven by the diffusion of methanol vapor into the PTCDI solution layer. The PTCDI molecules have low/no solubility in methanol and thus self-assemble into 1D nanostructures via π−π molecular stacking, resulting in an unconventional solvent-exchange crystallization process controlled by slow diffusion within a sealed container between the $CHCl_3$ solution of the PTCDI and the CH_3OH vapor. Molecules **1**−**3** were prepared by drop-casting 100 μL of PTCDI stock solution (1 mM in chloroform) directly onto the conductive surface of ITO (1 × 1 cm^2) and then vacuum drying at 50 °C for 30 min. The synthesized nanofibers are shown in Figure S4, and the samples were used for the following experiments (scanning electron microscopy (SEM), Raman spectroscopy, diffuse reflectance spectroscopy (DRS), photocurrent measurements, cyclic voltammetry (CV), electron paramagnetic resonance (EPR) spectroscopy, and photoelectrocatalytic hydrogen production).

2.2. Characterizations. The morphologies of the nanofibers were determined by SEM (JEOL 6700F). UV−vis DRS spectra were recorded on a Solid Spec-3700 DUV spectrophotometer and were converted from reflection to absorption by the Kubelka−Munk method. Raman spectra was recorded at room temperature by using a laser Raman spectrometer (LabRAM HR Evolution RAMAN SPECTROMETER, HORIBA Scientific Ltd.) with an Ar^+ laser (20 mW, 532 nm) as the excitation source. UV−vis absorption spectra were measured by a UV−vis spectrophotometer (UV-1800, Shimadzu, Japan). EPR spectra were measured by a Bruker A-300EPR X-band spectrometer.

2.3. Photoelectrochemical Analysis. The electrochemical measurements were carried out on an electrochemical workstation (CHI760C, Chenhua, China) with a conventional three-electrode cell. The photocurrent responses of the samples as the light was turned on and off were measured at 0.0 V. In the experiments, the prepared working electrode (described below) was positioned in the middle of a 0.1 M Na_2SO_4 aqueous solution with the sample side facing the incident light. A platinum net (1.5 × 1.5 cm^2) and a Ag/AgCl electrode were used as the counter electrode and reference electrode, respectively. When performing the photocurrent and CV experiments, a Xe lamp equipped with a 420 nm cutoff filter was used as the visible-light source.

Working electrodes were prepared by self-assembling PTCDI nanofibers on an ITO surface as described in Experimental section 2.1.3. The volume of the PTCDI stock solution used for the self-assembly process on each ITO glass surface was constant (100 μL of 1 mM stock solution in chloroform) in all experiments to ensure the same amount of PTCDI nanofibers on each ITO glass. For comparison, the same working electrodes of ITO glass were coated with PTCDI molecules **1**−**3** by adding 100 μL of 1 mM PTCDI stock solution (in chloroform) to the ITO glass and allowing the glass plates to dry in air. No fibril structure was formed during this quick casting and drying process. The molecular films formed in this manner were subjected to the same electrochemical and photoelectrocatalytic

DOI: 10.1021/acsami.8b05637
ACS Appl. Mater. Interfaces 2018, 10, 19764−19772

analyses under the same experimental conditions as were used for the nanofiber materials.

2.4. Photoelectrocatalytic Hydrogen Generation. Photoelectrocatalytic hydrogen generation experiments were performed in a custom three-electrode quartz reaction cell (Figure S1). A platinum net (1.5 × 1.5 cm^2) and a Ag/AgCl electrode were used as the counter electrode and reference electrode, respectively. The working electrodes were the same as those described above in Experimental section 2.3. A 0.2 M HCl aqueous solution (60 mL) was used as the electrolyte solution, and TEA (6 mL) was employed as a sacrificial agent for trapping holes. A 300 W Xe lamp (CEL-HXF300, AuLight, Beijing, China) with a band filter was used as the light source (≥420 nm). Because this study examines the half-reaction of H^+/H_2, a bias voltage of 0.60 V was utilized to drive the photogenerated electrons from the working electrode to the platinum electrode. Prior to all tests, the reaction vessel was repeatedly purged with argon for 30 min and placed under vacuum until no bubbles appeared; the reactor was then photoirradiated. The photocurrent was measured using an electrochemical analyzer (CHI760C, Chenhua, China). Quantitative analysis of hydrogen was carried out by gas chromatography (Agilent 7890A).

3. RESULTS AND DISCUSSION

The PTCDI D−A materials used in this study were fabricated in situ on ITO conductive glass surfaces through a solvent-vapor diffusion method that has been proven effective for promoting the self-assembly of molecules into well-defined nanofibers.[17] The nanofibers self-assembled from molecules **1**, **2**, and **3** were found to have similar morphologies, as shown by the SEM micrographs in Figure 1a,c,e. The average diameters of nanofibers **1**−**3** are approximately 245, 420, and 320 nm, respectively, and the lengths of the nanofibers are in the range of tens of microns. These thin nanofibers have a large surface area leading to a broad D−A interface, which facilitates the transfer of photoexcited electrons and effectively separates the charge carriers.[23] The strong $\pi-\pi$ stacking interactions between the perylene cores of adjacent molecules lead to effective π-electron delocalization and enhanced charge migration along the long axis of the nanofibers.[20] Finally, the separated charge carriers can be collected at the two electrodes following application of an electrical bias.

The Raman spectra of the PTCDI molecules and PTCDI nanofibers exhibit several Raman modes with frequencies of 1317, 1392, 1467, 1589, and 1604 cm^{-1} (Figure 2a), which are consistent with the PTCDI resonance Raman spectra reported in the literature.[34−36] As shown in Figure 2a, no significant changes in frequency were observed, indicating that the crystalline structure of the PTCDI molecules remains intact during self-assembly. Previous works by others and our laboratory have confirmed that the self-assembly of rigid planar π-conjugated molecules normally lead to the formation of highly crystalline materials dominated by 1D $\pi-\pi$ stacking interactions.[14] The 1604 cm^{-1} Raman-active normal mode corresponding to the in-plane C═C/C−C stretching/shrinking of the perylene aromatic ring core coupled to the C═O antisymmetric stretching is sensitive to the $\pi-\pi$ stacking intermolecular interactions.[19,37] The peaks at 1604 cm^{-1} in the Raman spectra of the three PTCDI nanofibers were more intense than the same peaks of the corresponding molecules. However, the intensity and frequency of the C−H in-plane bending band at 1317 cm^{-1} do not change following self-assembly.[19,37] These results suggested that the PTCDI nanofibers have a tight and ordered $\pi-\pi$ stacking structure.

The DRS spectra of monomeric PTCDI molecules normally show three pronounced peaks between 650 and 450 nm, which correspond to the 0−0, 0−1, and 0−2 electronic transitions,

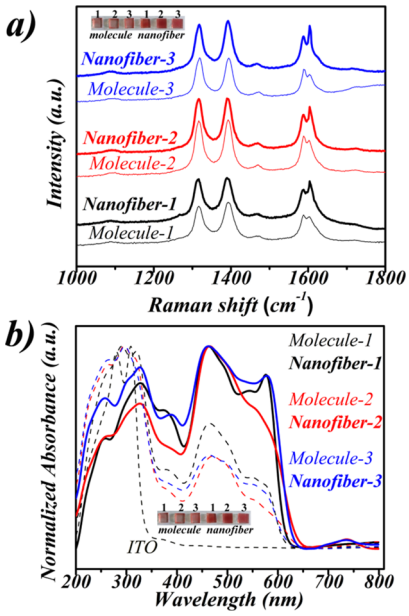

Figure 2. Raman (a) and UV−vis diffuse reflection (b) spectra measured on the drop-cast films of PTCDI molecules **1**−**3** and the corresponding nanofibers.

respectively.[38] Following the self-assembly of the PTCDI molecules into nanofibers, several changes can be observed in the DRS spectra (Figure 2b). A new peak emerges at 735 nm, and sharper, more pronounced peaks between 400 and 600 nm (most notably at 576 nm) are observed. The transitions from the ground state to the excited electronic states (0−0, 0−1, and 0−2) are dramatically enhanced upon aggregation. This spectral change indicates the PTCDI fibers have more organized $\pi-\pi$ stacking than the individual molecules prior to self-assembly.[39] The absorption of the PTCDI nanofibers was also red-shifted compared with the absorption of the single molecules of PTCDI; this observation is also consistent with the enhanced intermolecular interactions in the nanofibers. Enhanced absorption in visible region is conducive to the utilization of solar energy.

The 1D $\pi-\pi$ stacking of the perylene molecules within the nanofibers results in efficient charge transfer through π-electron delocalization along the long axis. Consequently, the PTCDI nanofibers exhibit strong photoconductivity.[18,20,21,40] The PTCDI nanofibers studied in this paper are stable to repeated cycles of illumination as shown by the consistent increase in photocurrent and subsequent decrease in photocurrent in light/dark cycles (Figure 3). Following illumination, the photocurrent increases rapidly and returns to the baseline level when the light is turned off. Compared with the drop-cast films of the PTCDI molecules, the self-assembled PTCDI nanofibers exhibit higher photocurrent response under the same illumination, indicating the organized intermolecular arrangement of building blocks results in enhanced charge separation and transport ability of the photogenerated charge carriers.

CV was also employed to investigate the electrochemical properties of the three PTCDI nanofibers. As shown in Figure S2, the CV plots revealed an amphoteric redox behavior. The characteristic reversible wave observed in all samples is due to two consecutive single-electron-transfer steps that occur between −0.2 and −0.8 V, which corresponds to two reversible one-electron reductions of the perylene diimide to the monoanionic and dianionic species.[41,42] During the CV

DOI: 10.1021/acsami.8b05637
ACS Appl. Mater. Interfaces 2018, 10, 19764−19772

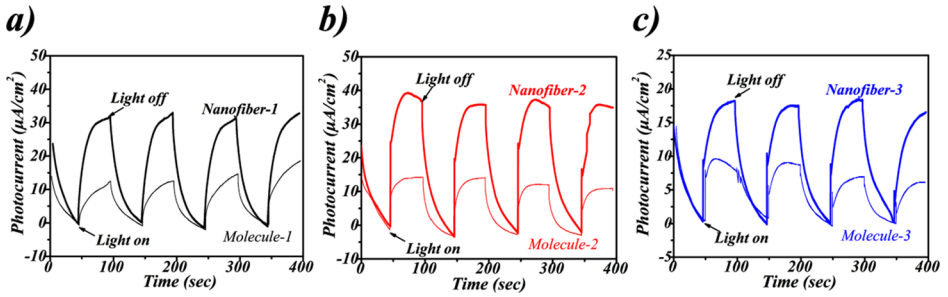

Figure 3. Repeated photocurrent responses measured over the ITO working electrodes coated with PTCDI molecule **1** (a), **2** (b), and **3** (c) under visible-light irradiation in 0.1 M Na_2SO_4 aqueous solution. The corresponding nanofibers assembled from molecules **1**−**3** were also tested for the same experiments with results shown in (a) to (c), respectively.

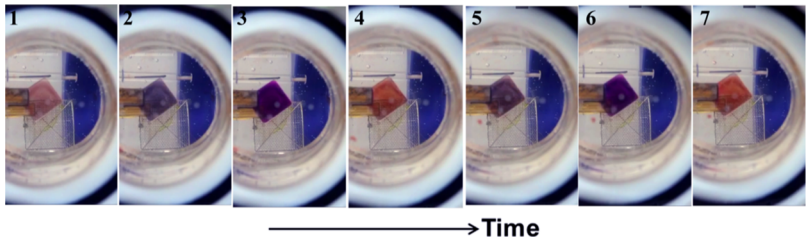

Figure 4. Still images of the video recorded of the electrochromic change in the PTCDI nanofibers of molecule **2** deposited an ITO glass. Photographs 1 to 7 show the two electrochromic cycle processes, as seen in the video provided in the Supporting Information. The color of the nanofibers changed from red to blue and then to violet as the reduction progressed to the radical monoanion and then to the dianion. The observed electrochromic color change was remarkably strong and reversible.

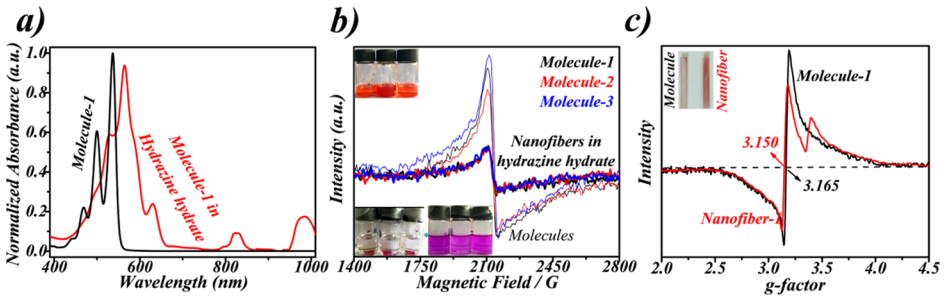

Figure 5. (a) UV−vis absorption spectra showing the formation of the anionic radical of the PTCDI by electron transfer reduction from hydrazine; the black spectrum is of the PTCDI molecular stock solution (molecule **1**, 0.5 mM in chloroform), and the red spectrum is of the reaction solution between the ITO glass with the nanofibers of **1** and 10 mL of hydrazine hydrate. (b) EPR spectra of the nanofibers assembled from molecules **1**−**3** (dissolved in an aqueous solution of hydrazine hydrate) compared with those from the corresponding molecules (1 mM PTCDI in pure chloroform). (c) Comparison of the EPR spectra of PTCDI molecule **1** and the corresponding nanofiber. The EPR spectra of molecules **2** and **3** are very similar to that of molecule **1**, but not shown in the figure for better clarity.

experiment, we observed that the reduction process was accompanied by a reversible electrochromic phenomenon in which the color of the nanofibers changed from red to blue during the first reduction and then to violet during the second reduction (see Figure 4 and the video clips in the Supporting Information). These electrochromic responses correspond to the reduction of perylene diimide and are in good agreement with the CV results.[18,43,44] The reversible color changes of the PTCDI nanofibers from red to blue and then to violet correspond to the neutral, radical anion, and dianion forms of the PTCDI unit.[45]

Efficient intermolecular electron transfer also occurs between the PTCDI nanofibers and reducing agents (e.g., hydrazine), leading to the formation of the soluble anionic radical of PTCDI.[17] When ITO glass coated with PTCDI nanofibers was immersed in an aqueous solution of hydrazine hydrate (80 wt %) under an argon atmosphere, reduction occurred as evidenced by the change in the color of the solution to violet. The PTCDI nanofibers, which are initially red, turned light blue and dissolved upon the addition of a small amount of hydrazine hydrate to the solution. Upon the addition of excess of hydrazine hydrate, the PTCDI solution turned deep purple because of the complete reduction of the PTCDI to its dianion. Furthermore, the reduction caused by hydrazine is reversible; when the solution was exposed to air, the PTCDI anionic radical was oxidized back to its neutral state as evidenced by the material returning to its initial red color (Figure S3). The UV−vis spectra also confirm the presence of anionic radicals in the presence of hydrazine hydrate (Figure 5a); the detection of the anionic radical implies the stable intramolecular π-delocalization of the charges over the whole PTCDI plane.[17,46] Such intramolecular π-delocalization can enhance the charge separation between the stacked molecules along a nanofiber. The anionic radical was also detected by EPR spectrometry. Solutions of the three PTCDI nanofibers dissolved in 15 mL of hydrazine hydrate (16.46 M) exhibited strong symmetric EPR

DOI: 10.1021/acsami.8b05637
ACS Appl. Mater. Interfaces 2018, 10, 19764−19772

signals (Figure 5b). The intensity of the radical anion signal in the hydrazine solution was significantly weaker than the signal of three PTCDI molecules in pure chloroform solutions. The decreased intensity of the EPR signal in the hydrazine solution is evidence of significant electron transfer from the hydrazine to the PTCDI molecules to form the dianion, which is EPR inactive. Moreover, the EPR spectra of the nanofibers assembled from the three PTCDI molecules lose the reflection symmetry about the center of the signal (Figure 5c), indicating an anisotropic **g**-tensor, with $g_{\perp}$ (3.165) > $g_{\parallel}$ (3.150). The anisotropic **g**-tensor is consistent with the uniaxial property of the nanofiber and indicative of intermolecular π-delocalization along the long axis of molecular stacking.[17]

The observed enhancement of photoinduced charge separation in the D−A nanofibers is exemplified by their ability to function efficiently in the photoelectrocatalytic generation of hydrogen gas in which an ITO conductive glass plate coated with PTCDI nanofibers was used as the working electrode (photoanode), a Ag/AgCl electrode was used as the reference electrode, and a 1.5 × 1.5 cm^2 platinum net was used as the counter electrode. A 0.2 M HCl aqueous solution was used as the electrolyte solution. Efficient charge separation is key to enhancing photocatalysis, and TEA was used as a sacrificial agent because the photoelectrocatalytic oxidation of organic sacrificial agents is known to produce higher photocurrents than water oxidation leading to higher hydrogen production rates.[47] The hydrogen production setup (shown in Figure S1) was maintained at 0.6 V versus the Ag/AgCl electrode under illumination with a xenon lamp ($\lambda \geq 420$ nm). A photoanode carrying the PTCDI nanofibers absorbs photons, producing electron−hole pairs. Electrons are collected by the photoanode and are conducted through an external circuit to the platinum electrode where they reduce protons to form hydrogen. Meanwhile, the photogenerated holes are scavenged by TEA through rapid oxidation, which significantly prevents the recombination of photogenerated electrons and holes.

Photoelectrocatalytic hydrogen generation was carried out for 4 h during which the photocurrent was monitored. The amount of hydrogen generated was measured at 1 h intervals using GC analysis of the headspace. Following an initial increase for each of the nanofibers, the photocurrents were nearly constant (Figure 6b); the sharp negative spikes are due to the removal of the samples at the end of each hour. Quantification of the amount of hydrogen present at the end of each hour showed steady-state hydrogen generation for all three nanofibers, as shown in Figure 6a. The photoelectrocatalysis using the three nanofibers was proven robust, as no significant decrease in catalyst efficiency was observed after three repeated tests of 8 h cycles (Figure 6d). Notably, nanofibers of molecules **2** and **3** demonstrate significantly different efficiencies in hydrogen production (Figure 6c) even though these two molecules possess electron-donating groups with very similar pKa values and electron donating strength.[48−50] The observed difference in catalysis efficiency is likely due to the variations in molecular stacking, which in turn affect the configurational constraints between the donor group and the PTCDI backbone and thus the charge transfer and separation.[51] The lower catalysis efficiency of the nanofiber of **1** would be due to the flexible linear alkyl linker, which may cause an offset in the stacking between molecules, weakening the intermolecular charge transport. The observation reported in this work opens a number of avenues for future studies on the structure−property−function relationship of photoelectrocatalysts with regard to the molecular design for improving efficiency. Additionally, the hydrogen production was proportional to the observed photocurrent although we did not achieve 100% Faradaic efficiency (see the Supporting Information for the description of the calculation of the Faradaic efficiency). The efficiencies of hydrogen generation using the nanofiber electrodes in this study were approximately 27−30% of the Faradaic efficiency. The difference in the theoretical and actual efficiencies of hydrogen production may be due to the low efficiency of hydrogen collection.

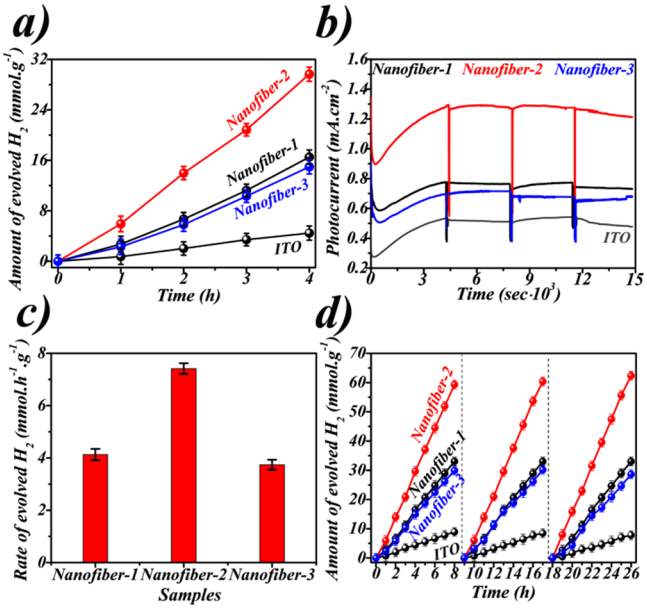

Figure 6. (a) Time dependence of hydrogen production via photoelectrocatalysis during the 4 h experiment. (b) Photocurrent versus time recorded during the photoelectrocatalysis. (c) Hydrogen production rate estimated for each of the nanofibers from the slope of the linear fitting of (a). (d) Repeated tests of the photoelectrocatalytic hydrogen production over the three PTCDI nanofibers.

Considering the acidic electrolyte, the structure of the nanofibers may be changed due to protonation during the hydrogen production process. To verify this structural change, the morphologies of the three nanofibers were examined by SEM imaging as shown in Figure S5. The micrographs showed no significant morphology changes in the three nanofibers, indicating that the PTCDI nanofibers are sufficiently robust for photoelectrocatalytic hydrogen production in acidic electrolytes. Considering the micrometer-scale thickness of the nanofibers, each nanofiber contains multiple columnar stacks of molecules. Molecular protonation can only occur on the outermost surface molecules (and likely only on the side that protrudes away from the glass), so the effect of protonation on the electronic properties of the whole nanofiber should be minimal as the photoinduced electron transfer can occur from any donor moiety inside the nanofiber.[48−50] Nonetheless, the PTCDI nanofiber catalysts employed in this study exhibited higher efficiencies than have been reported for other visible-light active photocatalysts[29−31] as shown in Table 1, which presents some recent literature data for comparison.[52−58]

On the basis of the aforementioned results, we proposed a possible mechanism to explain the high photoelectrocatalytic hydrogen production efficiency of the three nanofibers, as illustrated in Scheme 2. Recent studies have demonstrated that effective charge transfer from the donor groups to the PTCDI

DOI: 10.1021/acsami.8b05637
ACS Appl. Mater. Interfaces 2018, 10, 19764−19772

Table 1. Comparison between the Data of This Work and the Recent Literature Data on Photoelectrocatalytic Hydrogen Production

photocatalyst	electrolyte	current density (mA cm^2)	bias (V)	H_2 generation rate (μmol min^{-1})	Faradaic yield	refs
$Cu_2O/NiO/Cu_2MoS_4$	$Na_2SO_4/NaHSO_4$ (pH = 5)		0.3 (RHE)		32−18%	56
Cu_2O/NiO	$Na_2SO_4/NaHSO_4$ (pH = 5)		0.3 (RHE)		23−17%	56
$Cu/nanoCu_2O/NiO$	Na_2SO_4 (pH = 6)		−0.36 (NHE)		32 ± 6%	58
TiO_2	H_2SO_4	0.15		0.045		57
$Ti\text{-}Fe_2O_3$	NaOH	2.2	0.7 (Ag/AgCl)	1.2		53
$Cu\text{-}Ni/TiO_2$	KOH			1.58		54
CdS	Na_2SO_4	0.167		0.71		52
Pd/TNT	KOH	1.1		0.47		55
CoS/planar n^+−p-Si	potassium phosphate buffer (pH = 7)	1.3		0.05 mL min^{-1}	100%	59
Mo_3S_4/p-Si	pH = 0	9	0 (RHE)		100%	60
MoS_2/planar n^+−p-Si	pH = 0		−0.1 (RHE)	0.217	100%	61
Co dithiolene polymer/p-Si	pH = 1.3 H_2SO_4		−0.12 (RHE)		80% (±3%)	62
NiO/CdSe/CoP	pH = 6.8 Na_2SO_4	0.11	−0.2 (RHE)		81%	63
$Ni/CuO_2/CuO$	pH = 5	4.3	0 (RHE)		84%	64
nanofiber **1**−**3**	HCl	0.7−1.3	0.6 (Ag/AgCl)	4−8 μmol h^{-1} g^{-1}	27−30%	this work

Scheme 2. (a) Photogenerated Electrons are Delocalized Along the Nanofiber and can be Trapped by the Surface-Adsorbed Electron Acceptors. (b) With Visible-Light Irradiation and an Applied Bias Voltage, Photogenerated Electrons Rapidly Migrate Along the Long Axis of the Nanofibers and Then are Transported Along the External Circuit to the Pt Electrode, Which Minimizes the Internal Recombination of the Electron/Hole Pairs; The Electrons Accumulated at the Pt Electrode Reduce Protons to Form Hydrogen

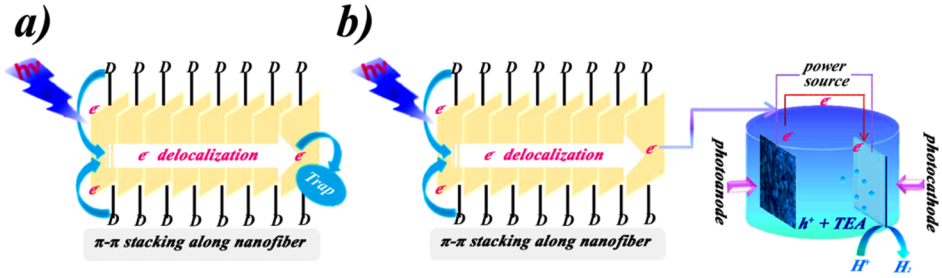

backbone generates anionic radicals and results in considerable enhancement of the electronic conductivity.[21] In this study, the PTCDI-based D−A interface was prepared by symmetrically attaching electron-donating groups at both imide positions of the PTCDI cores (Scheme 1). Photoinduced charge separation can be understood as exciton dissociation at the intramolecular D−A interface, producing e^- and h^+ charge carriers with the electron being stabilized within the large planar π-conjugation system of PTCDI.[23] The $\pi-\pi$ stacking along the nanofiber further facilitates the intermolecular delocalization of the electron, enhancing the charge separation (Scheme 2a).[23] Upon application of a bias voltage, the electrons are driven along the nanofibers and then through the external circuit to the Pt electrode where they go on to reduce protons to form hydrogen (Scheme 2b).

4. CONCLUSION

In conclusion, three PTCDI molecules were synthesized by symmetrically placing electron donors at both imide positions. Nanofibers assembled from these PTCDI molecules all featured well-defined morphologies and exhibited strong photocurrents. The magnitude of the photocurrent was strongly affected by the molecular structure and rigidity of the donor group, and the nanofiber of molecule **2** was the most conductive. Interestingly, a strong and reversible electrochromic color change was observed during CV. The color of the nanofibers changed from red to blue and then to violet as the reduction progressed to the radical monoanion and then to the dianion. This series of one-electron reductions was confirmed by UV absorption, EPR spectroscopy and hydrazine reduction.

Most importantly, when deposited onto ITO glass electrodes, these nanofibers functioned as effective visible-light catalysts for hydrogen production under photoelectrocatalysis. The nanofiber of molecule **2** was the most effective catalyst and showed 30% of the Faradaic efficiency. The nanofibers produced hydrogen at a steady-state for more than 8 h and afforded repeatable results for three consecutive testing cycles. The high efficiency, reproducibility and durability all bode well for their potential application in hydrogen production and other relevant solar energy utilization systems.

■ ASSOCIATED CONTENT

Supporting Information

The Supporting Information is available free of charge on the ACS Publications website at DOI: 10.1021/acsami.8b05637.

DOI: 10.1021/acsami.8b05637
ACS Appl. Mater. Interfaces 2018, 10, 19764−19772

Calculation process of Faradaic efficiency for hydrogen generation; diagram of the experimental setup for photoelectrocatalytic hydrogen production; CV plots of molecules and corresponding nanofibers; the video recorded for electrochromism change in the nanofiber **1**−**3**; photograph showing one set of experiments validating the electrochromic change; the photographs of molecules **1**−**3** and nanofibers **1**−**3** all from ITO; and SEM images of the nanofibers **1**−**3** after reaction (PDF)

Video recorded for electrochromism change in the nanofiber-1 (AVI)

Video recorded for electrochromism change in the nanofiber-2 (AVI)

Video recorded for electrochromism change in the nanofiber-3 (AVI)

AUTHOR INFORMATION

Corresponding Authors

*E-mail: wangyh@ms.xjb.ac.cn (Y.W.).
*E-mail: cywang@ms.xjb.ac.cn (C.W.).
*E-mail: lzang@eng.utah.edu. Phone: +86-0991-3835879. Fax: +86-0991-3838957 (L.Z.).

ORCID

Chuanyi Wang: 0000-0002-7146-115X

Notes

The authors declare no competing financial interest.

ACKNOWLEDGMENTS

This work was supported by the National Natural Science Foundation of China (grant nos. 21473248 and 21421004), the CAS/SAFEA International Partnership Program for Creative Research Teams, and the NSF (CBET 1502433).

REFERENCES

(1) Hains, A. W.; Liang, Z.; Woodhouse, M. A.; Gregg, B. A. Molecular Semiconductors in Organic Photovoltaic Cells. *Chem. Rev.* **2010**, *110*, 6689−6735.

(2) Sirringhaus, H. Organic Semiconductors: An Equal-Opportunity Conductor. *Nat. Mater.* **2003**, *2*, 641−642.

(3) Samuel, I. D. W.; Turnbull, G. A. Organic Semiconductor Lasers. *Chem. Rev.* **2007**, *107*, 1272−1295.

(4) Coakley, K. M.; McGehee, M. D. Conjugated Polymer Photovoltaic Cells. *Chem. Mater.* **2004**, *16*, 4533−4542.

(5) Gross, M.; Müller, D. C.; Nothofer, H.-G.; Scherf, U. Improving the Performance of Doped π-Conjugated Polymers for Use in Organic Light-Emitting Diodes. *Nature* **2000**, *405*, 661.

(6) Zhao, D.; Wu, Q.; Cai, Z.; Zheng, T.; Chen, W.; Lu, J.; Yu, L. Electron Acceptors Based on α-Substituted Perylene Diimide (PDI) for Organic Solar Cells. *Chem. Mater.* **2016**, *28*, 1139−1146.

(7) Allard, S.; Forster, M.; Souharce, B.; Thiem, H.; Scherf, U. Organic Semiconductors for Solution-Processable Field-Effect Transistors (OFETs). *Angew. Chem., Int. Ed.* **2008**, *47*, 4070−4098.

(8) Kirner, J. T.; Stracke, J. J.; Gregg, B. A.; Finke, R. G. Visible-Light-Assisted Photoelectrochemical Water Oxidation by Thin Films of a Phosphonate-Functionalized Perylene Diimide Plus CoO_x Cocatalyst. *ACS Appl. Mater. Interfaces* **2014**, *6*, 13367−13377.

(9) Weingarten, A. S.; Kazantsev, R. V.; Palmer, L. C.; McClendon, M.; Koltonow, A. R.; Samuel, A. P. S.; Kiebala, D. J.; Wasielewski, M. R.; Stupp, S. I. Self-Assembling Hydrogel Scaffolds for Photocatalytic Hydrogen Production. *Nat. Chem.* **2014**, *6*, 964−970.

(10) Melkonyan, F. S.; Zhao, W.; Drees, M.; Eastham, N. D.; Leonardi, M. J.; Butler, M. R.; Chen, Z.; Yu, X.; Chang, R. P. H.; Ratner, M. A.; Facchetti, A. F.; Marks, T. J. Bithiophenesulfonamide Building Block for π-Conjugated Donor−Acceptor Semiconductors. *J. Am. Chem. Soc.* **2016**, *138*, 6944−6947.

(11) Roncali, J. Molecular Bulk Heterojunctions: An Emerging Approach to Organic Solar Cells. *Acc. Chem. Res.* **2009**, *42*, 1719−1730.

(12) Facchetti, A. π-Conjugated Polymers for Organic Electronics and Photovoltaic Cell Applications. *Chem. Mater.* **2011**, *23*, 733−758.

(13) Wang, C.; Dong, H.; Hu, W.; Liu, Y.; Zhu, D. Semiconducting π-Conjugated Systems in Field-Effect Transistors: A Material Odyssey of Organic Electronics. *Chem. Rev.* **2012**, *112*, 2208−2267.

(14) Chen, S.; Slattum, P.; Wang, C.; Zang, L. Self-Assembly of Perylene Imide Molecules into 1D Nanostructures: Methods, Morphologies, and Applications. *Chem. Rev.* **2015**, *115*, 11967−11998.

(15) Kozma, E.; Catellani, M. Perylene Diimides Based Materials for Organic Solar Cells. *Dyes Pigments* **2013**, *98*, 160−179.

(16) Li, C.; Wonneberger, H. Perylene Imides for Organic Photovoltaics: Yesterday, Today, and Tomorrow. *Adv. Mater.* **2012**, *24*, 613−636.

(17) Zang, L.; Che, Y.; Moore, J. S. One-Dimensional Self-Assembly of Planar π-Conjugated Molecules: Adaptable Building Blocks for Organic Nanodevices. *Acc. Chem. Res.* **2008**, *41*, 1596−1608.

(18) Wu, N.; Zhang, Y.; Wang, C.; Slattum, P. M.; Yang, X.; Zang, L. Thermoactivated Electrical Conductivity in Perylene Diimide Nanofiber Materials. *J. Phys. Chem. Lett.* **2017**, *8*, 292−298.

(19) Wang, J.; Shi, W.; Liu, D.; Zhang, Z.; Zhu, Y.; Wang, D. Supramolecular Organic Nanofibers with Highly Efficient and Stable Visible Light Photooxidation Performance. *Appl. Catal., B* **2017**, *202*, 289−297.

(20) Wu, N.; Wang, C.; Slattum, P. M.; Zhang, Y.; Yang, X.; Zang, L. Persistent Photoconductivity in Perylene Diimide Nanofiber Materials. *ACS Energy Lett.* **2016**, *1*, 906−912.

(21) Wu, N.; Wang, C.; Bunes, B. R.; Zhang, Y.; Slattum, P. M.; Yang, X.; Zang, L. Chemical Self-Doping of Organic Nanoribbons for High Conductivity and Potential Application as Themiresistive Sensor. *ACS Appl. Mater. Interfaces* **2016**, *8*, 12360−12368.

(22) Wang, C.; Bunes, B. R.; Xu, M.; Wu, N.; Yang, X.; Gross, D. E.; Zang, L. Interfacial Donor−Acceptor Nanofibril Composites for Selective Alkane Vapor Detection. *ACS Sens.* **2016**, *1*, 552−559.

(23) Zang, L. Interfacial Donor−Acceptor Engineering of Nanofiber Materials to Achieve Photoconductivity and Applications. *Acc. Chem. Res.* **2015**, *48*, 2705−2714.

(24) Kazantsev, R. V.; Dannenhoffer, A. J.; Weingarten, A. S.; Phelan, B. T.; Harutyunyan, B.; Aytun, T.; Narayanan, A.; Fairfield, D. J.; Boekhoven, J.; Sai, H.; Senesi, A.; O'Dogherty, P. I.; Palmer, L. C.; Bedzyk, M. J.; Wasielewski, M. R.; Stupp, S. I. Crystal-Phase Transitions and Photocatalysis in Supramolecular Scaffolds. *J. Am. Chem. Soc.* **2017**, *139*, 6120−6127.

(25) Chen, S.; Jacobs, D. L.; Xu, J.; Li, Y.; Wang, C.; Zang, L. 1D Nanofiber Composites of Perylene Diimides for Visible-Light-Driven Hydrogen Evolution from Water. *RSC Adv.* **2014**, *4*, 48486−48491.

(26) Liu, D.; Wang, J.; Bai, X.; Zong, R.; Zhu, Y. Self-Assembled PDINH Supramolecular System for Photocatalysis Under Visible Light. *Adv. Mater.* **2016**, *28*, 7284−7290.

(27) Ding, C.; Shi, J.; Wang, Z.; Li, C. Photoelectrocatalytic Water Splitting: Significance of Cocatalysts, Electrolyte, and Interfaces. *ACS Catal.* **2016**, *7*, 675−688.

(28) Sprick, R. S.; Jiang, J.-X.; Bonillo, B.; Ren, S.; Ratvijitvech, T.; Guiglion, P.; Zwijnenburg, M. A.; Adams, D. J.; Cooper, A. I. Tunable Organic Photocatalysts for Visible-Light-Driven Hydrogen Evolution. *J. Am. Chem. Soc.* **2015**, *137*, 3265−3270.

(29) Tee, S. Y.; Win, K. Y.; Teo, W. S.; Koh, L.-D.; Liu, S.; Teng, C. P.; Han, M.-Y. Recent Progress in Energy-Driven Water Splitting. *Adv. Sci.* **2017**, *4*, 1600337.

(30) Roger, I.; Shipman, M. A.; Symes, M. D. Earth-Abundant Catalysts for Electrochemical and Photoelectrochemical Water Splitting. *Nat. Rev. Chem.* **2017**, *1*, 0003.

(31) Landman, A.; Dotan, H.; Shter, G. E.; Wullenkord, M.; Houaijia, A.; Maljusch, A.; Grader, G. S.; Rothschild, A. Photoelectrochemical

DOI: 10.1021/acsami.8b05637
ACS Appl. Mater. Interfaces 2018, 10, 19764−19772

Water Splitting in Separate Oxygen and Hydrogen Cells. *Nat. Mater.* **2017**, *16*, 646−651.
(32) Christoforidis, K. C.; Fornasiero, P. Photocatalytic Hydrogen Production: A Rift into the Future Energy Supply. *ChemCatChem* **2017**, *9*, 1523−1544.
(33) Okemoto, A.; Kishishita, K.; Maeda, S.; Gohda, S.; Misaki, M.; Koshiba, Y.; Ishida, K.; Horie, T.; Taniya, K.; Ichihashi, Y.; Nishiyama, S. Application of Picene Thin-Film Semiconductor as a Photocatalyst for Photocatalytic Hydrogen Formation from Water. *Appl. Catal., B* **2016**, *192*, 88−92.
(34) Angelella, M.; Wang, C.; Tauber, M. J. Resonance Raman Spectra of a Perylene Bis(dicarboximide) Chromophore in Ground and Lowest Triplet States. *J. Phys. Chem. A* **2013**, *117*, 9196−9204.
(35) Castiglioni, C.; Tommasini, M.; Zerbi, G. Raman Spectroscopy of Polyconjugated Molecules and Materials: Confinement Effect in One and Two Dimensions. *Philos. Trans. R. Soc., A* **2004**, *362*, 2425−2459.
(36) Scholz, R.; Kobitski, A. Y.; Kampen, T. U.; Schreiber, M.; Zahn, D. R. T.; Jungnickel, G.; Elstner, M.; Sternberg, M.; Frauenheim, T. Resonant Raman Spectroscopy of 3,4,9,10-Perylene-Tetracarboxylic-Dianhydride Epitaxial Film. *Phys. Rev. B: Condens. Matter Mater. Phys.* **2000**, *61*, 13659.
(37) Singh, R.; Giussani, E.; Mróz, M. M.; Di Fonzo, F.; Fazzi, D.; Cabanillas-González, J.; Oldridge, L.; Vaenas, N.; Kontos, A. G.; Falaras, P.; Grimsdale, A. C.; Jacob, J.; Müllen, K.; Keivanidis, P. E. On the Role of Aggregation Effects in the Performance of Perylene-Diimide Based Solar Cells. *Org. Electron.* **2014**, *15*, 1347−1361.
(38) Balakrishnan, K.; Datar, A.; Oitker, R.; Chen, H.; Zuo, J.; Zang, L. Nanobelt Self-Assembly from an Organic n-Type Semiconductor: Propoxyethyl-PTCDI. *J. Am. Chem. Soc.* **2005**, *127*, 10496−10497.
(39) Balakrishnan, K.; Datar, A.; Naddo, T.; Huang, J.; Oitker, R.; Yen, M.; Zhao, J.; Zang, L. Effect of Side-Chain Substituents on Self-Assembly of Perylene Diimide Molecules: Morphology Control. *J. Am. Chem. Soc.* **2006**, *128*, 7390−7398.
(40) Draper, E. R.; Walsh, J. J.; McDonald, T. O.; Zwijnenburg, M. A.; Cameron, P. J.; Cowan, A. J.; Adams, D. J. Air-Stable Photoconductive Films Formed from Perylene Bisimide Gelators. *J. Mater. Chem. C* **2014**, *2*, 5570−5575.
(41) Michot, C.; Baril, D.; Armand, M. Polyimide-Polyether Mixed Conductors as Switchable Materials for Electrochromic Devices. *Sol. Energy Mater. Sol. Cells* **1995**, *39*, 289−299.
(42) Lu, W.; Gao, J. P.; Wang, Z. Y.; Qi, Y.; Sacripante, G. G.; Duff, J. D.; Sundararajan, P. R. Electrochemical Characterization, Electrochroism, and Voltage-Dependent Fluorescence of Novel Perylene-Containing Polyimides. *Macromolecules* **1999**, *32*, 8880−8885.
(43) Beaujuge, P. M.; Ellinger, S.; Reynolds, J. R. The Donor-Acceptor Approach Allows a Black-to-Transmissive Switching Polymeric Electrochrome. *Nat. Mater.* **2008**, *7*, 795−799.
(44) Blanco, R.; Gómez, R.; Seoane, C.; Segura, J. L.; Mena-Osteritz, E.; Bäuerle, P. An Ambipolar Peryleneamidine Monoimide-Fused Polythiophene with Narrow Band Gap. *Org. Lett.* **2007**, *9*, 2171−2174.
(45) Marcon, R. O.; Brochsztain, S. Highly Stable 3, 4, 9, 10−Perylenediimide Radical Anions Immobilized in Robust Zirconium Phosphonate Self-Assembled Films. *Langmuir* **2007**, *23*, 11972−11976.
(46) Wang, J.; He, E.; Liu, X.; Yu, L.; Wang, H.; Zhang, R.; Zhang, H. High Performance Hydrazine Vapor Sensor Based on Redox Mechanism of Twisted Perylene Diimide Derivative with Lower Reduction Potential. *Sens. Actuators, B* **2017**, *239*, 898−905.
(47) Lianos, P. Review of Recent Trends in Photoelectrocatalytic Conversion of Solar Energy to Electricity and Hydrogen. *Appl. Catal., B* **2017**, *210*, 235−254.
(48) Tang, C.; Smith, A. M.; Collins, R. F.; Ulijn, R. V.; Saiani, A. Fmoc-Diphenylalanine Self-Assembly Mechanism Induces Apparent pKa Shifts. *Langmuir* **2009**, *25*, 9447−9453.
(49) Adams, D. J.; Mullen, L. M.; Berta, M.; Chen, L.; Frith, W. J. Relationship Between Molecular Structure, Gelation Behaviour and Gel Properties of Fmoc-Dipeptides. *Soft Matter* **2010**, *6*, 1971.
(50) Nolan, M. C.; Walsh, J. J.; Mears, L. L. E.; Draper, E. R.; Wallace, M.; Barrow, M.; Dietrich, B.; King, S. M.; Cowan, A. J.; Adams, D. J. pH Dependent Photocatalytic Hydrogen Evolution by Self-Assembled Perylene Bisimides. *J. Mater. Chem. A* **2017**, *5*, 7555−7563.
(51) Holman, M. W.; Liu, R.; Zang, L.; Yan, P.; DiBenedetto, S. A.; Bowers, R. D.; Adams, D. M. Studying and Switching Electron Transfer: From the Ensemble to the Single Molecule. *J. Am. Chem. Soc.* **2004**, *126*, 16126−16133.
(52) Liang, X.; Liu, J.; Zeng, D.; Li, C.; Chen, S.; Li, H. Hydrogen Generation Promoted by Photocatalytic Oxidation of Ascorbate and Glucose at a Cadmium Sulfide Electrode. *Electrochim. Acta* **2016**, *198*, 40−48.
(53) Kalamaras, E.; Dracopoulos, V.; Sygellou, L.; Lianos, P. Electrodeposited Ti-Doped Hematite Photoanodes and Their Employment for Photoelectrocatalytic Hydrogen Production in the Presence of Ethanol. *Chem. Eng. J.* **2016**, *295*, 288−294.
(54) Bashiri, R.; Mohamed, N. M.; Kait, C. F.; Sufian, S.; Kakooei, S.; Khatani, M.; Gholami, Z. Optimization Hydrogen Production over Visible Light-Driven Titania-Supported Bimetallic Photocatalyst from Water Photosplitting in Tandem Photoelectrochemical Cell. *Renewable Energy* **2016**, *99*, 960−970.
(55) Zhang, Y.; Zhao, G.; Shi, H.; Zhang, Y.-n.; Huang, W.; Huang, X.; Wu, Z. Photoelectrocatalytic Glucose Oxidation to Promote Hydrogen Production over Periodically Ordered TiO_2 Nanotube Arrays Assembled of Pd Quantum Dots. *Electrochim. Acta* **2015**, *174*, 93−101.
(56) Yang, C.; Tran, P. D.; Boix, P. P.; Bassi, P. S.; Yantara, N.; Wong, L. H.; Barber, J. Engineering a $Cu_2O/NiO/Cu_2MoS_4$ Hybrid Photocathode for H_2 Generation in Water. *Nanoscale* **2014**, *6*, 6506−6510.
(57) Seger, B.; Lu, G. Q.; Wang, L. Electrical Power and Hydrogen Production from a Photo-Fuel Cell Using Formic Acid and Other Single-Carbon Organics. *J. Mater. Chem.* **2012**, *22*, 10709.
(58) Lin, C.-Y.; Lai, Y.-H.; Mersch, D.; Reisner, E. Cu_2OlNiO_x Nanocomposite as an Inexpensive Photocathode in Photoelectrochemical Water Splitting. *Chem. Sci.* **2012**, *3*, 3482.
(59) Sun, Y.; Liu, C.; Grauer, D. C.; Yano, J.; Long, J. R.; Yang, P.; Chang, C. J. Electrodeposited Cobalt-Sulfide Catalyst for Electrochemical and Photoelectrochemical Hydrogen Generation from Water. *J. Am. Chem. Soc.* **2013**, *135*, 17699−17702.
(60) Hou, Y.; Abrams, B. L.; Vesborg, P. C. K.; Björketun, M. E.; Herbst, K.; Bech, L.; Setti, A. M.; Damsgaard, C. D.; Pedersen, T.; Hansen, O.; Rossmeisl, J.; Dahl, S.; Nørskov, J. K.; Chorkendorff, I. Bioinspired Molecular Co-Catalysts Bonded to a Silicon Photocathode for Solar Hydrogen Evolution. *Nat. Mater.* **2011**, *10*, 434−438.
(61) Ding, Q.; Meng, F.; English, C. R.; Cabán-Acevedo, M.; Shearer, M. J.; Liang, D.; Daniel, A. S.; Hamers, R. J.; Jin, S. Efficient Photoelectrochemical Hydrogen Generation Using Heterostructures of Si and Chemically Exfoliated Metallic MoS_2. *J. Am. Chem. Soc.* **2014**, *136*, 8504−8507.
(62) Downes, C. A.; Marinescu, S. C. Efficient Electrochemical and Photoelectrochemical H<sub>2 Production from Water by a Cobalt Dithiolene One-Dimensional Metal−Organic Surface. *J. Am. Chem. Soc.* **2015**, *137*, 13740−13743.
(63) Meng, P.; Wang, M.; Yang, Y.; Zhang, S.; Sun, L. CdSe Quantum Dots/Molecular Cobalt Catalyst Co-Grafted Open Porous NiO Film as a Photocathode for Visible Light Driven H_2 Evolution from Neutral Water. *J. Mater. Chem. A* **2015**, *3*, 18852−18859.
(64) Dubale, A. A.; Pan, C.-J.; Tamirat, A. G.; Chen, H.-M.; Su, W.-N.; Chen, C.-H.; Rick, J.; Ayele, D. W.; Aragaw, B. A.; Lee, J.-F.; Yang, Y.-W.; Hwang, B.-J. Heterostructured Cu_2O/CuO Decorated with Nickel as a Highly Efficient Photocathode for Photoelectrochemical Water Reduction. *J. Mater. Chem. A* **2015**, *3*, 12482−12499.

DOI: 10.1021/acsami.8b05637
ACS Appl. Mater. Interfaces 2018, 10, 19764−19772